Resolution of redundancy in robots and in a human arm

Ashitava Ghosal *

Abstract

The author obtained his Ph D in 1986 under Professor Bernard Roth. In a publication from the research, it was shown that the redundant joints in a serial robot could be used to make the end-effector linear velocity distribution isotropic. In this work we revisit those results, present recent results on how redundancy is made use of in a human arm, and finally attempt to link the earlier work with new results. The human arm can be modeled as a redundant serial manipulator and the redundancy can be computed from the null-space of the Jacobian matrix. In a recent work, healthy adults were made to perform point-to-point reaching tasks in eight directions first without any disturbance, then with an applied force and finally with the force switched off. Statistical analyses show that trajectory and reaching errors due to the applied force die out with trials and subjects who explore the redundancy in the arm adapt faster to the external force. It is also shown that the anisotropy in the error distribution reduces with trials. These new results suggest that the redundancy in a human arm is used to reduce trajectory errors and anisotropy arising out of external disturbances.

Keywords: Redundant robots, Optimization, Human arm, Exploration, Motor Learning.

1 Introduction

To position and orient a rigid body in three dimensional space, one needs to specify six parameters – three for position and three for orientation. A consequence of this fact is that a six degree-of-freedom robot, with six independently actuated joints, can arbitrarily position and orient an end-effector or an object carried by the end-effector in three-dimensional space. However from early days, robots with more than six actuated joints have been built and in biological systems, more than the required number of actuated joints is ubiquitous. Such systems are known as redundant systems and a key problem in redundant systems is that for a specified position and orientation of the end-effector, there exists infinitely many possibilities for the actuated joints. To choose one particular set, also known as *resolution* of redundancy, researchers have proposed many strategies and extensive research continues to be done. One of the earliest proposed use of redundancy was to overcome the constraints on motion of the robot end-effector due to the presence of joint limits [1] and to avoid obstacles and singularities present in the workspace of a robot [2]. Some of the strategies, such as obstacle avoidance and avoiding wrist singularities were implemented on a seven degree-of-freedom prototype robot [3] and on a prototype wrist with four joints [4]. The key mathematical tool used by most of the researchers in the 80's was the Moore-Penrose generalized inverse[5], also called the *pseudo-inverse*, of the manipulator Jacobian matrix. The manipulator Jacobian matrix relates the end-effector linear and angular velocities to the joint rates and for

*Corresponding Author, Professor, Department of Mechanical Engineering, Indian Institute of Science, Bangalore, India. Email: asitava@iisc.ac.in

a redundant robot, the manipulator Jacobian matrix is *rectangular*. Hence, for a prescribed end-effector linear and angular velocity, the Jacobian matrix cannot be inverted to obtain the joint rates. In its basic form, the use of the pseudo-inverse of the Jacobian matrix can be shown to minimize the sum of squares of the joint rates for a given linear and angular velocity of the end-effector. The pseudo-inverse of the manipulator Jacobian matrix were also used to minimize joint acceleration, used with weighting matrices to minimize joint torques and extended to include a null-space term which could be used to optimize additional quantities such as a manipulability index (see the review paper by Klein and Huang[6] and textbook by Nakamura[7] and the reference contained in them for details of various pseudo-inverse based resolution schemes in redundant robots). The pseudo-inverse based approaches are numerical in nature and provide results at the level of joint velocities – they do not provide any insight or give deeper understanding at the level of position or orientation of the end-effector. The pseudo-inverse involves obtaining the inverse of a matrix and this has a complexity of $\mathcal{O}(n^4)$ where n is the number of joint variables. Hence it is not very efficient for modeling and simulation of hyper-redundant systems which have a much larger number of links and actuated joints – examples of a hyper-redundant systems are"snake" robots[8], models of continuum robots [9], and classical models of proteins [10] with chains of amino acids during folding.

To overcome some of the difficulties in the pseudo-inverse based approach, researchers proposed an approach where the central 'backbone' of a hyper-redundant manipulator is approximated with a continuous curve. The redundancy is resolved by updating the curve for a desired motion of the end-effector and at every step *fitting* a robot with rigid links and joints. In reference [11], the backbone curves was chosen as linear combination of modes and as splines in reference [12]. In this approach, since the continuous curve is used for motion planning the axial *length* of the curve and as a consequence the length of the hyper-redundant manipulator is not preserved.

A third resolution scheme for hype-redundant manipulators, based on the classical *tractrix* curve, was proposed in reference [13]. Unlike the joint space pseudo-inverse based schemes, this is a Cartesian space scheme. For a prescribed Cartesian motion of the tip of the first link of the hyper-redundant robot (termed as the 'head'), the Cartesian motion of the end of the first link (termed the 'tail') is computed according to the closed-form equations of the tractrix curve. The motion of the 'head' of the second link is then set to the motion of the 'tail' of the first link and again the motion of the 'tail' of the second link is computed according to the equations of the tractrix curve. Proceeding in a similar way, the Cartesian motion of all the links of the hyper-redundant robot is obtained. Once the Cartesian motion is obtained, the rotations at the joints can be obtained from simple trigonometry and vector algebra. It is shown in reference [13] that the tractrix based approach has a complexity of $\mathcal{O}(n)$ and, more interestingly, the motion along the chain dies out as one traverses the chain from the end-effector to the other end. This property makes the motion of the entire hyper-redundant manipulator more natural. In a series of papers, the author and his students have used the tractrix based approach to perform real-time and realistic simulations of one-dimensional flexible objects such as ropes and hyper-redundant manipulators [14], compared the pseudo-inverse, modal and tractrix based approaches on a 8 link planar hyper-redundant robot [15], shown that the tractrix solution results from a general variational problem where a functional defining the

infinitesimal motion of the points on a continuous curve is minimized subject to preservation of the arc length of the curve (for a straight line segment, the velocity of the 'tail' lies along the straight line segment [16]), used splines and the tractrix based approach to obtain efficient algorithms for simulation and rendering of the motion of flexible one-dimensional objects [17] and, finally, shown that the tractrix based approach can be extend to include obstacle avoidance [18].

The linear and angular velocity distribution of an end-effector in a serial manipulator is governed by the nonlinear kinematic equations. It has been known that the velocity distribution is not uniform and some directions are easier to move than others [19]. In reference [20], the authors had proposed a redundancy resolution scheme where a redundant joint rate was chosen in a particular way to make the end-effector velocity distribution *isotropic*. In this work, we revisit this approach and bring out its key features – this is the content of section 2. In section 3, an experiment on point-to-point reaching along randomly chosen eight directions in a plane, conducted by healthy human subjects, is presented. A model of the redundant human arm is considered and an approach to quantify the redundancy present in the human arm model, using the null-space of the Jacobian matrix, is proposed. When a lateral disturbing force is applied during the reaching tasks, the error in the trajectory initially increases and as the trials progress, the error reduces. In section 3, from statistical analyses, it is shown that subjects who explore redundancy during the un-perturbed motion, learn how to reduce the error arising out of the disturbance faster. It is also shown that errors in certain directions are consistently larger and the anisotropy in the error distribution decreases with the trials. Taken together these new results suggest that redundancy in human arm is used for learning how to deal with perturbations and one possible mechanism of reducing trajectory errors is by reducing the anisotropy in error inherently present in the point-to-point reaching tasks. Section 4 presents the conclusion of this work.

2 Resolution of redundancy and isotropy

In this section, we present the notion of velocity distribution of the end-effector of a serial robot and the approach to use the redundancy to make the velocity distribution isotropic. More details are available in references [19, 20].

2.1 Velocity ellipse

Consider a simple planar two-degree-of-freedom manipulator with two rotary joints as shown in figure 1. The end-effector point (x, y) can be written in terms of link lengths l_1, l_2 and the joint angles θ_1 and θ_2 as

$$\begin{aligned} x &= l_1 \cos\theta_1 + l_2 \cos(\theta_1 + \theta_2) \\ y &= l_1 \sin\theta_1 + l_2 \sin(\theta_1 + \theta_2) \end{aligned} \tag{1}$$

The velocity of the end-effector point (x, y), denoted by $\mathbf{V}$, is given by

$$\mathbf{V} \triangleq \begin{pmatrix} \dot{x} \\ \dot{y} \end{pmatrix} = \begin{bmatrix} -l_1 \sin\theta_1 - l_2 \sin(\theta_1 + \theta_2) & -l_2 \sin(\theta_1 + \theta_2) \\ l_1 \cos\theta_1 + l_2 \cos(\theta_1 + \theta_2) & l_2 \cos(\theta_1 + \theta_2) \end{bmatrix} \begin{pmatrix} \dot{\theta_1} \\ \dot{\theta_2} \end{pmatrix} \tag{2}$$

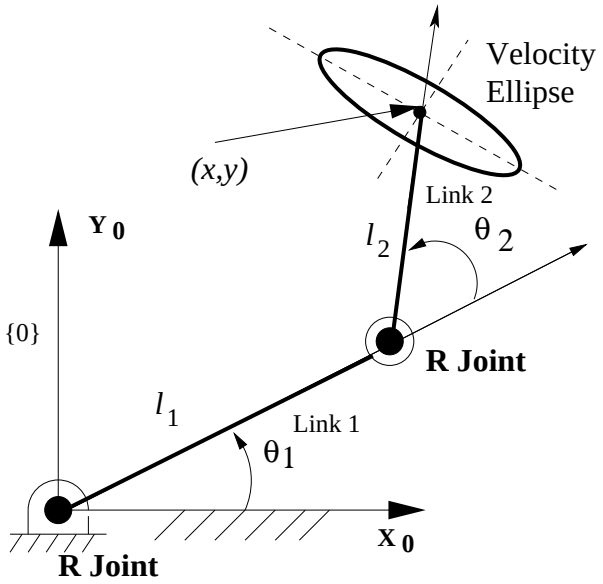

Figure 1: A planar 2R manipulator and velocity ellipse

where $\dot{\theta}_1$, $\dot{\theta}_2$ are the joint rates at the two rotary joints, and the 2×2 matrix inside the square brackets is the Jacobian matrix $[J(\mathbf{\Theta})]$ for the planar manipulator described in a fixed reference frame $\{0\}$ – $\mathbf{\Theta}$ denotes the vector of joint rotations $(\theta_1, \theta_2)^T$ for the planar manipulator with two rotary (R) joints. The dot product of the linear velocity vector with itself can be written as

$$\mathbf{V}^2 \triangleq \mathbf{V} \cdot \mathbf{V} = g_{11}\dot{\theta}_1^2 + 2g_{12}\dot{\theta}_1\dot{\theta}_2 + g_{22}\dot{\theta}_2^2 \tag{3}$$

where $g_{ij},\ i,j = 1,2$, are the elements of a matrix $[\ g\ ] = [J(\mathbf{\Theta})]^T[J(\mathbf{\Theta})]$. For the planar 2R manipulator the g_{ij}'s are

$$\begin{aligned} g_{11} &= l_1^2 + l_2^2 + 2l_1l_2c_2 \\ g_{12} = g_{21} &= l_2^2 + l_1l_2c_2 \\ g_{22} &= l_2^2 \end{aligned} \tag{4}$$

It may be noted that the elements g_{11} and g_{12}, for the planar 2R manipulator, are functions of θ_2 alone and g_{22} is a constant. For arbitrary $\dot{\theta}_1$ and $\dot{\theta}_2$, any $\mathbf{V}$ can be obtained, i.e., the linear velocity vector spans the complete $\Re^2$. To obtain a more geometric insight, we obtain the maximum and minimum of $\mathbf{V}^2$ subject to a constraint, $\dot{\theta}_1^2 + \dot{\theta}_2^2 = 1$. These can be obtained by solving $\partial \mathbf{V}^{*2}/\partial\dot{\theta}_i = 0$, $i = 1,2$, where

$$\mathbf{V}^{*2} = g_{11}\dot{\theta}_1^2 + 2g_{12}\dot{\theta}_1\dot{\theta}_2 + g_{22}\dot{\theta}_2^2 - \lambda(\dot{\theta}_1^1 + \dot{\theta}_2^2 - 1)$$

Performing the partial differentiation reduces to an eigenvalue problem

$$[\ g\ ]\dot{\mathbf{\Theta}} - \lambda\dot{\mathbf{\Theta}} = 0 \tag{5}$$

and the eigenvalues are given by

$$\lambda_{1,2} = (1/2)\{(g_{11} + g_{22}) \pm [(g_{11} + g_{22})^2 - 4(g_{11}g_{22} - g_{12}^2)]^{1/2}\} \tag{6}$$

Since [g] is real, symmetric and positive definite, the eigenvalues are always real and positive, and assuming $\lambda_1 > \lambda_2$, the maximum and minimum values of $|\mathbf{V}|$ are

$$|\mathbf{V}|_{\max} = \sqrt{\lambda_1}, \quad |\mathbf{V}|_{\min} = \sqrt{\lambda_2} \tag{7}$$

It may be noted that if a constraint $\dot{\theta}_1^2 + \dot{\theta}_2^2 = k^2$ is used, then the maximum and minimum $|\mathbf{V}|$ are scaled by k.

From the relationship $\mathbf{V} = [J(\mathbf{\Theta})]\dot{\mathbf{\Theta}}$, we can also write (dropping the dependence of $\mathbf{\Theta}$ for convenience)

$$[J]^T\mathbf{V} = [\ g\ ]\dot{\mathbf{\Theta}}$$

and for non-singular [g], we can get

$$\mathbf{V}^T([J][\ g\ ]^{-1})([J][\ g\ ]^{-1})^T\mathbf{V} = \dot{\mathbf{\Theta}}^T\dot{\mathbf{\Theta}}$$

For the planar 2R manipulator, the matrix $([J][\ g\ ]^{-1})([J][\ g\ ]^{-1})^T$ is symmetric and of rank 2. Hence if $\dot{\mathbf{\Theta}}^T\dot{\mathbf{\Theta}} = 1$, the above equation reduces to $(\dot{x}, \dot{y})^T([J][\ g\ ]^{-1})([J][\ g\ ]^{-1})^T(\dot{x}, \dot{y}) = 1$. From linear algebra, we know that an expression of the form $\mathbf{x}^T[A]\mathbf{x} = 1$, with $[A]$ symmetric and non-singular, describes an ellipse. Hence, we conclude that the tip of the linear velocity vector traces an *ellipse* and the semi-major and semi-minor axes of the ellipse are $\sqrt{\lambda_1}$ and $\sqrt{\lambda_2}$, respectively. It may be noted that the size of the ellipse will be scaled by k if a constraint $\dot{\mathbf{\Theta}}^T\dot{\mathbf{\Theta}} = k^2$ is used, but the shape of the ellipse does not change with k.

For the planar 2R manipulator, the eigenvalues of [g] are only functions of θ_2 and hence the shape and size of the ellipse will be different for different values of θ_2. For the planar 2R manipulator, we show the ellipse traced by the tip of the linear velocity vector in figure 1. The velocity ellipse is generated for $l_1 = 1.5$, $l_2 = 1.0$, $\theta_1 = 30^\circ$ and $\theta_2 = 60^\circ$, the major and minor axis are 0.9727, 0.2323, the centre of the ellipse is at $(1.299, 1.757)$ with the minor axis inclined at an angle 1.0261 rad from the horizontal.

The shape of the velocity ellipse indicates which directions are 'easier' for the end-effector to move for given joint rates – the magnitude of the linear velocity vector is larger along the major axis of the ellipse and hence it is easier to move along the major axis as compared to the minor axis. If the ellipse reduces to a circle, then it is equally easy to move in all directions. All points in the workspace, where the ellipse is a circle, are called *isotropic* and this concept was first developed by Salisbury[21]. In general, a manipulator is said to be in an isotropic configuration if the eigenvalues of $[J(\mathbf{\Theta})]$ or [g] are equal. For the planar 2R manipulator, the eigenvalues of [g] are equal only if

$$g_{11} = g_{12} \quad \text{and} \quad g_{12} = 0 \tag{8}$$

From the expressions of g_{ij}'s given in equation (4), the above conditions imply that

$$l_1^2 + 2l_1l_2\cos\theta_2 = 0 \quad \text{and} \quad l_2^2 + l_1l_2\cos\theta_2 = 0$$

and this is only possible if

$$l_1 = \sqrt{2}l_2 \quad \text{and} \quad \cos\theta_2 = -\frac{1}{\sqrt{2}} \tag{9}$$

Equation (9) implies that a planar 2R manipulator can posses isotropic configurations *only* if the link lengths have a ratio of $\sqrt{2}$, and for these link dimensions, the second joint should be at an angle of 135°. Since θ_1 can take any value between $[0, 2\pi]$, all the isotropic configurations lie on a circle.

The above idea of a velocity ellipse can be easily extended to spatial motion. For spatial manipulators with two degrees of freedom, the locus of the end-effector position traces a surface in $\Re^3$. In this case, the tip of the linear velocity vector lies in the *tangent* plane at any point on the surface, and the velocity ellipse lies on this tangent plane. If the manipulator has three degrees of freedom and the motion is in $\Re^3$, the Jacobian matrix maps a unit sphere in $\dot{\mathbf{\Theta}}$ space to a *velocity ellipsoid* in $\Re^3$. The shape and size of the linear velocity ellipsoid can again be obtained from the eigenvalues of [g] which will now be a 3×3 matrix.

2.2 Redundant 3R planar manipulator

Consider a planar 3R robot as shown in figure 2. The forward kinematic equations relating the end-effector point (x, y) in terms of the joint variables θ_1, θ_2 and θ_3 are given as

$$\begin{aligned} x &= l_1 \cos\theta_1 + l_2 \cos(\theta_1 + \theta_2) + l_3 \cos(\theta_1 + \theta_2 + \theta_3) \\ y &= l_1 \sin\theta_1 + l_2 \sin(\theta_1 + \theta_2) + l_3 \sin(\theta_1 + \theta_2 + \theta_3) \end{aligned} \tag{10}$$

Unlike the planar 2R example earlier, for a given (x, y) one cannot obtain an unique or finitely many $\theta_i,\ i = 1, 2, 3$ and we have a redundant system. As mentioned in section 1, there are various approaches to resolve the redundancy and obtain an unique inverse kinematics solution. In the following we revisit the approach described in reference[20].

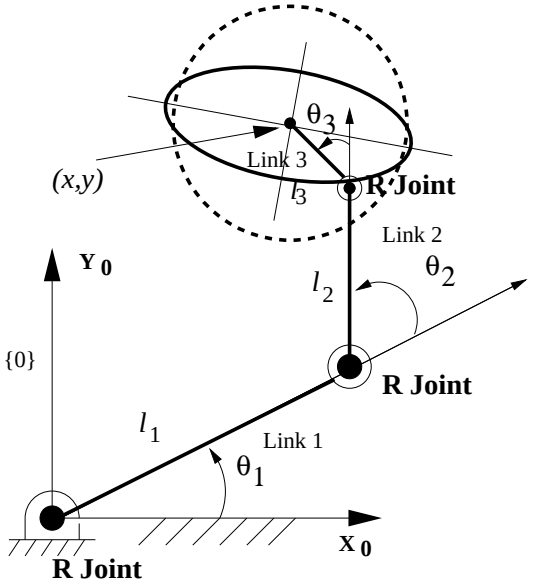

Figure 2: A planar 3R manipulator – velocity ellipse and circle

The Jacobian matrix for the planar 3R robot is 2×3 and can be written as

$$[J(\mathbf{\Theta})] = \begin{bmatrix} -l_1 s_1 - l_2 s_{12} - l_3 s_{123} & -l_2 s_{12} - l_3 s_{123} & -l_3 s_{123} \\ l_1 c_1 + l_2 c_{12} + l_3 c_{123} & l_2 c_{12} + l_3 c_{123} & l_3 c_{123} \end{bmatrix} \tag{11}$$

where $c_{(\cdot)}$, $s_{(\cdot)}$ denote cosine and sine of the angle $(\cdot)$ and c_{12}, s_{12} etc. denote $\cos(\theta_1+\theta_2)$, $\sin(\theta_1+\theta_2)$ etc., respectively. The linear velocity of the end-effector can be written as

$$\mathbf{V} \triangleq \begin{pmatrix} \dot{x} \\ \dot{y} \end{pmatrix} = \sum_{i=1}^{3} \mathbf{\Psi}_i \dot{\theta}_i \tag{12}$$

where $\mathbf{\Psi}_i$ is the i^{th} column of $[J(\mathbf{\Theta})]$ given above.

Following[20], we assume that

$$\mathbf{\Psi}_3 \dot{\theta}_3 = \alpha_1 \mathbf{\Psi}_1 \dot{\theta}_1 + \alpha_2 \mathbf{\Psi}_2 \dot{\theta}_2 \tag{13}$$

where α_1 and α_2 are non-zero. Taking dot product of equation (13) with $\mathbf{\Psi}_1$ and $\mathbf{\Psi}_2$, and simplifying we can obtain

$$\begin{aligned} \alpha_1 &= \frac{[(\mathbf{\Psi}_3 \cdot \mathbf{\Psi}_1)g_{22} - (\mathbf{\Psi}_3 \cdot \mathbf{\Psi}_2)g_{12}]\dot{\theta}_3}{(g_{11}g_{22} - g_{12}^2)\dot{\theta}_1} = a_1(\dot{\theta}_3/\dot{\theta}_1) \\ \alpha_2 &= \frac{[(\mathbf{\Psi}_3 \cdot \mathbf{\Psi}_2)g_{11} - (\mathbf{\Psi}_3 \cdot \mathbf{\Psi}_1)g_{12}]\dot{\theta}_3}{(g_{11}g_{22} - g_{12}^2)\dot{\theta}_2} = a_2(\dot{\theta}_3/\dot{\theta}_2) \end{aligned} \tag{14}$$

where $g_{ij} = \mathbf{\Psi}_i \cdot \mathbf{\Psi}_j,\ i = 1, 2$. The expression for the linear velocity of the end-effector can now be written as

$$\mathbf{V} = \sum_{i=1}^{2} (1 + \alpha_i)\mathbf{\Psi}_i \dot{\theta}_i \tag{15}$$

Substituting equation (13) in equation (12), we can obtain an expression for $\mathbf{V}^2$ similar to equation (3) and we can get

$$\begin{aligned} g'_{11} &= (1+\alpha_1)^2 \mathbf{\Psi}_1 \cdot \mathbf{\Psi}_1 = (1+\alpha_1)^2 g_{11} \\ g'_{12} &= (1+\alpha_1)(1+\alpha_2)\mathbf{\Psi}_1 \cdot \mathbf{\Psi}_2 = (1+\alpha_1)(1+\alpha_2) g_{12} \\ g'_{22} &= (1+\alpha_2)^2 \mathbf{\Psi}_2 \cdot \mathbf{\Psi}_2 = (1+\alpha_2)^2 g_{22} \end{aligned} \tag{16}$$

The eigenvalues of $[\ g'\ ]$ are functions of α_1 and α_2 and are *equal* when

$$\begin{aligned} \alpha_2 &= \frac{\pm(g_{11}/g_{22})^{1/2} - 1}{1 \mp (g_{11}/g_{22})^{1/2}[(a_1\dot{\theta}_2)/(a_2\dot{\theta}_1)]} \\ \alpha_1 &= (a_1\dot{\theta}_2/a_2\dot{\theta}_1)\alpha_2 \end{aligned} \tag{17}$$

and using $\dot{\theta}_1^2 + \dot{\theta}_2^2 = 1$, we get

$$\dot{\theta}_3^2 = [(a_1/\alpha_1)^2 + (a_2/\alpha_2)^2]^{-1} \tag{18}$$

From the analysis it is clear that $\dot{\theta}_3$ computed as in equation (18) will result in an *isotropic* velocity distribution and all directions are equally 'easy' to move. Figure 2 shows the velocity ellipse when $\dot{\theta}_3$ is not computed according to equation (18) while the velocity distribution is a circle when $\dot{\theta}_3$ is computed as in equation (18). The velocity distributions shown in figure 2 was obtained for $l_1 = 1.5$, $l_2 = 1.0$, $l_3 = 0.8$, and at the location given by $\theta_1 = 30°$, $\theta_2 = 90°$ and $\theta_3 = 45°$. The major and the minor axes of the ellipse are 1.0594 and 0.4078, respectively.

It may be mentioned that we need not have started from equation (13) and expressed $\mathbf{\Psi}_3\dot{\theta}_3$ in terms of $\mathbf{\Psi}_1\dot{\theta}_1$ and $\mathbf{\Psi}_2\dot{\theta}_2$. We can also express $\mathbf{\Psi}_1\dot{\theta}_1$ or $\mathbf{\Psi}_2\dot{\theta}_2$ in terms of the other two and arrive at similar expressions for $\dot{\theta}_1$ or $\dot{\theta}_2$ to make the velocity distribution isotropic.

3 Resolution of redundancy in human arm

Figure 3 shows a schematic of a human arm. As shown the human arm, including the wrist and ignoring the fingers, can be modeled with 7 degrees of freedom – a three degree-of-freedom (DOF) joint at the shoulder and two DOF joints at the elbow and wrist. Unlike a robot, one joint in a human arm could be actuated by several muscles – for example, the elbow joint is known to be actuated by 7 muscles and there is *redundancy* in actuation. In this work, however, we do not consider the redundancy in the actuation and focus on joint redundancy alone. In this section, we present an experimental approach to get an insight into how the redundancy is resolved in the human arm when it is used for point-to-point reaching tasks. Details of this work is available in references [22, 23].

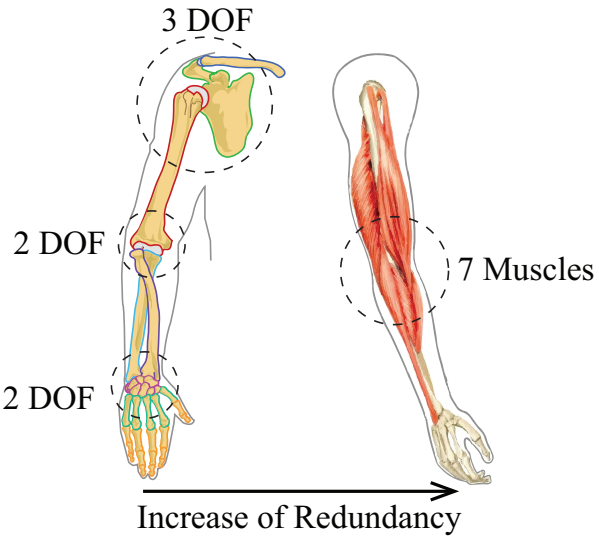

Figure 3: Schematic of a human arm and muscles

3.1 Experimental set-up and reaching task

Figure 4 (a) shows the main components in the experimental set-up. An healthy adult sits on a chair in a dark room with the head immobilized and the chin resting on a Chin Rest. He/she holds a planar Robotic Arm which can be moved along 8 directions (45° apart). The robot can be programmed to be free or apply a desired force along the trajectory. The motion of the robot end-effector (and the hand) is projected on an inverted a flat screen Monitor and the subject can see the motion of the robot end-effector (and the hand) as a movement of a cursor (through appropriate programming) on the Semi-silvered Mirror. The subject can only see this cursor motion and *not* his/her hand during motion and this is to avoid direct visual feedback of any part of the hand trajectory during the experiment. At the start of the experiment, a fixation box is shown at the centre of the screen and then randomly one target box in one of the eight directions, at a distance of 15 cm, is shown (see figure 4(b)). The subject has to move his/her hand, grasping the robot end-effector, to reach the shown target box and if the target box is reached, the trial is recorded as a success. The subject is instructed to move as fast as possible although a time interval of more than

approximately 1 second for one trial is not counted as a success – this is to avoid roaming along the trajectory. Although industrial robots can move much faster, from a neuro-science perspective the motion of about 15 cm in one second is fast enough to be classified as dynamic.

The arm of the human subject is fitted with 7 electromagnetic sensors [24] which measure position and orientation of the locations where they are fixed and these measurements are then used to compute the human arm joint angles. The (x, y) motion of the robot end-effector (and the hand) is also recorded in the robot controller.

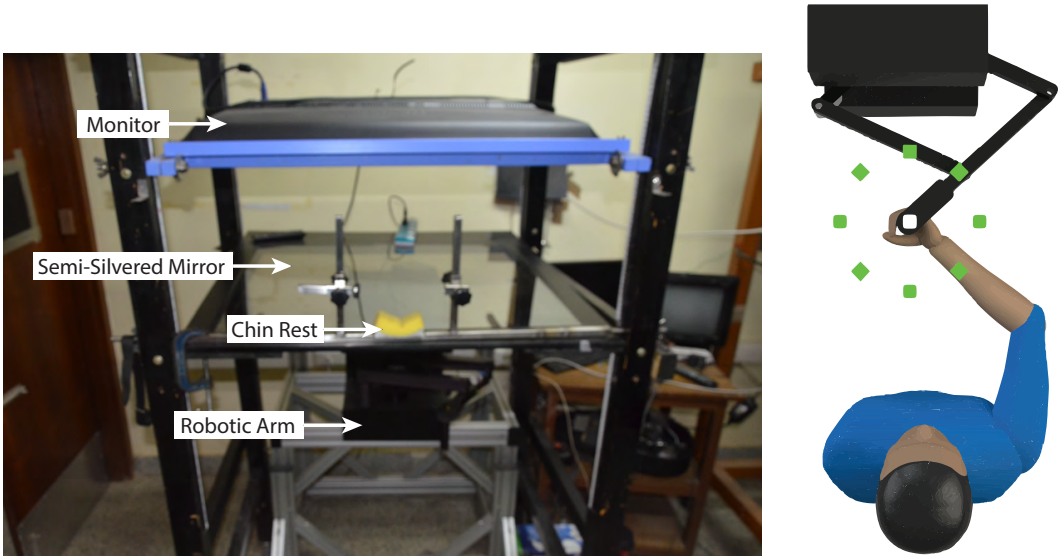

(a) Main components (b) Reaching task along 8 directions

Figure 4: Experimental set-up (from [23])

The point-to-point reaching task is divided into three phases as shown in figure 5. In the initial about 100 trials, termed as "Baseline" when the target box is shown on the screen, the hand and the robot are moved to reach that target box and then come back to the central fixation box. In the second phase, a lateral force is applied by the robot to the hand during its motion. The force is proportional to the velocity of the hand and is given as

$$\begin{bmatrix} F_x \\ F_y \end{bmatrix} = \begin{bmatrix} 0 & -K \\ K & 0 \end{bmatrix} \begin{bmatrix} \dot{x} \\ \dot{y} \end{bmatrix} \tag{19}$$

where F_x, F_y correspond to the forces exerted by the robotic arm, $\dot{x}$, $\dot{y}$ correspond to the velocity components of hand and K is a constant and equal to 20 Ns/m. This lateral force disturbs the hand trajectory and the trajectory become curved. In about 200 trials, the error in trajectory is reduced and the trajectory becomes straighter. In the third phase of about 100 trials, termed "Washout", the lateral force is switched off.

The trajectories of the hand (as computed from the sensors and recorded in the robot controller) are shown in figure 6. The panel labeled 'A' shows the trajectories of the hand during the "Baseline" where no external disturbance is applied by the robot. Panel B shows the first 5 curved hand trajectories when the lateral force is applied and panel C shows the hand trajectories when the lateral force is switched off. The fact that the curvature of the hand trajectory becomes opposite when the force is switched off implies that the subject has learned to adapt to the lateral force

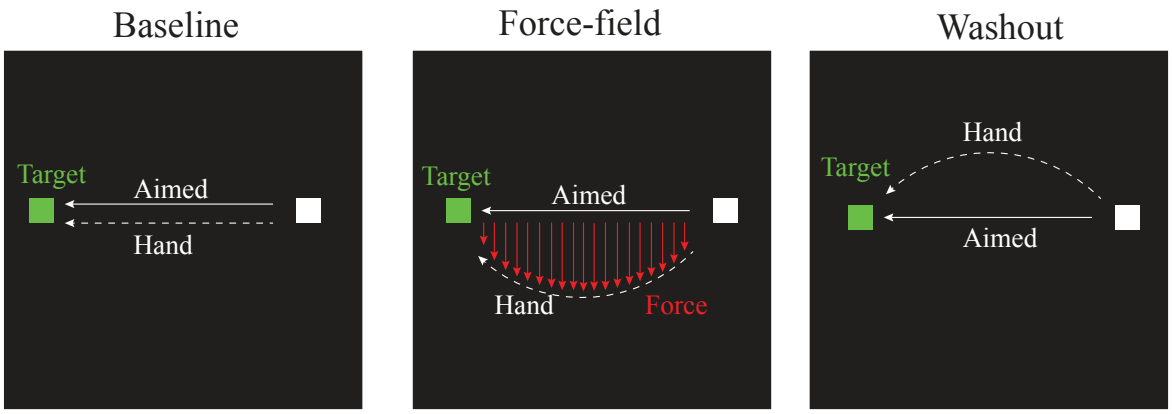

Figure 5: Three phases of reaching trials (from [23])

disturbance. Panel D plots the error at the peak velocity of the hand for a subject. The error in different directions of motion has the same colour code as in panel A. We can make the following observation from errors shown in panel D:

- The error in the "Baseline" is small when compared to the initial trials with the force. The errors are also large initially when the force is switched off.
- As the trials progresses, the errors with the force applied reduces. Likewise in the "Washout" phase the errors become small quickly.
- One can fit exponential curves to obtain a learning rate. The error $e(n)$ at trial number n can be written as

$$e(n) = a \exp(-\beta\ n) \tag{20}$$

where a is a constant and β is the learning rate. The use of an exponent fit is motivated by the standard learning rule which is a first-order process that depends on the current error. The goodness of fit, r^2 value, for a population of 10 subjects was found to be 0.93 and hence β was used as a metric to quantify the learning rate for each subject. The solid black curves in panel D shows the exponential fit.

To quantify the redundancy in the human arm during the point-to-point *planar* movements, we assume a model of the human arm as shown in figure 7. The model is different from the human arm shown in figure 3 in two main ways – a) due to the experimental set-up the portion of the body above the shoulder also moves and we need to take into account this motion, and b) the motion of the robot and the hand is purely planar. These two aspects can be taken into account if we assume four joint angles, θ_{clavicle}, θ_{shoulder}, θ_{elbow} and θ_{wrist}, in the forward kinematic model. Denoting these angles by θ_1, θ_2, θ_3 and θ_4, respectively, we can write the location of the hand as

$$\begin{aligned} x &= l_1 \cos\theta_1 + l_2 \cos\theta_2 + l_3 \cos\theta_3 + l_4 \cos\theta_4 \\ y &= l_1 \sin\theta_1 + l_2 \sin\theta_2 + l_3 \sin\theta_3 + l_4 \sin\theta_4 \end{aligned} \tag{21}$$

The above equations represent a planar 4R redundant manipulator and is similar to equations (1) and (10) – the key difference being that the angles are absolute since the sensors measure absolute

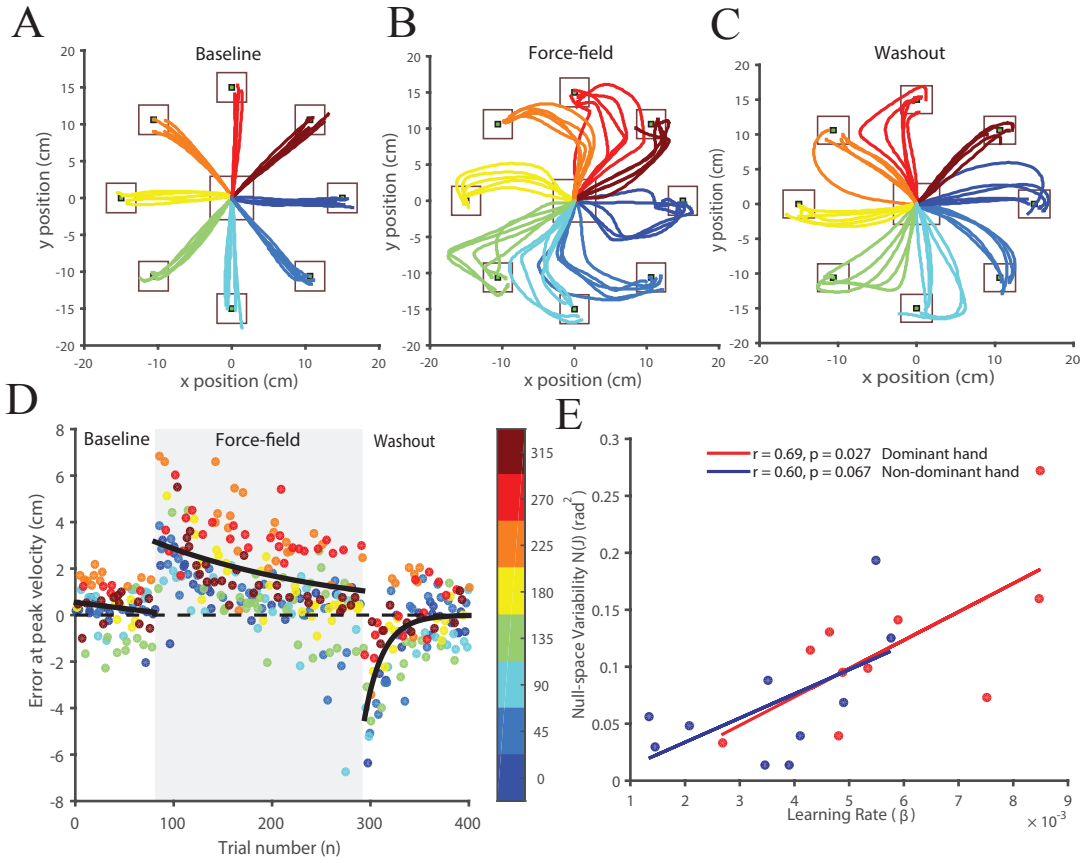

Figure 6: Results from point-to-point reaching task [22]

orientation. The link lengths $l_i,\ i = 1, 2, 3, 4$ are computed from the data from the sensors placed in the arm and vary a little with different subjects – for the results shown in panel A through D, the link lengths of the individual are 5.65 cm, 13.39 cm, 26.85 cm, 5.19 cm, respectively. It maybe noted that the link lengths are not the distances between the joints as shown in figure 3. To ensure that the l_i values are valid, the (x, y) obtained from equation (21) is compared with the (x, y) values of the robot end-effector and it was found that for this individual, the difference was less than 1.0 %.

The above forward kinematic model represents a redundant system and we cannot have a unique nominal $(\theta_1, \theta_2, \theta_3, \theta_4)^T$ vector (denoted by $\mathbf{\Theta}$) for any point-to-point (x, y) reaching tasks. We assume that the average $\bar{\mathbf{\Theta}}$, obtained from the measurements of the joints in the "Baseline" period, is the nominal $\mathbf{\Theta}$. We compute the difference between $\bar{\mathbf{\Theta}}$ and the measured $\mathbf{\Theta}$ for a trial k, at the peak velocity, and we can write

$$\Delta\mathbf{\Theta}_k = \bar{\mathbf{\Theta}} - \mathbf{\Theta}_k \tag{22}$$

Based on the forward kinematic model, the Jacobian matrix of the planar 4R robot, at the peak velocity, can be obtained as

$$[J(\bar{\mathbf{\Theta}})] = \begin{bmatrix} -l_1 s_1 & -l_2 s_2 & -l_3 s_3 & -l_4 s_4 \\ l_1 c_1 & l_2 c_2 & l_3 c_3 & l_4 c_4 \end{bmatrix} \tag{23}$$

The null-space of $[J(\bar{\mathbf{\Theta}})]$ is two-dimensional and a point in the null-space represents changes in joint configurations which *do not* change the mean hand position (x, y). The null-space of $[J(\bar{\mathbf{\Theta}})]$

can be obtained as a solution of

$$[J(\bar{\mathbf{\Theta}})]\xi_i = 0, \quad i = 1, 2 \tag{24}$$

For each trial, the sum of the component of $\Delta\mathbf{\Theta}_k$ along the null-space directions, $\xi_i,\ i = 1, 2$, is given by

$$\mathbf{\Theta}_R = \sum_{i=1}^{2} \langle \Delta\mathbf{\Theta}_k, \xi_i \rangle\ \xi_i \tag{25}$$

and we quantify the redundancy in the human arm model as the square of the magnitude of $\mathbf{\Theta}_R$ across all the trials divided by the number of trials n. Mathematically, this is written as

$$N(J) = \sum_{i=1}^{n} \frac{(\mathbf{\Theta}_R)^2}{n} \tag{26}$$

and the scalar $N(J)$ is a measure of the redundancy of the human arm performing point-to-point reaching tasks in the "Baseline" phase.

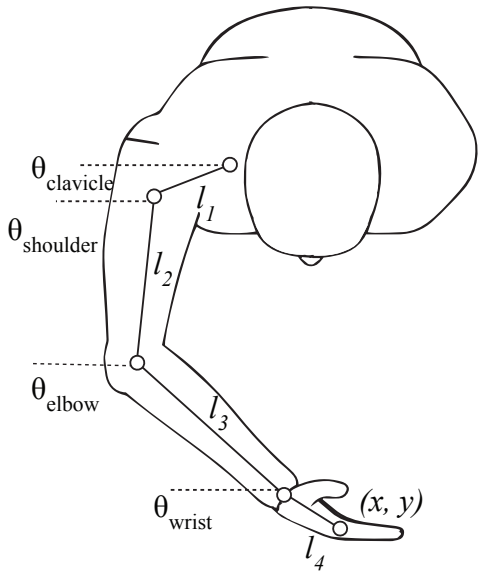

Figure 7: Kinematic model of the human arm for planar motion

Panel E in figure 6 shows a plot of the "Baseline" null-space variability or redundancy $N(J)$ and the learning rate for the 10 subjects obtained during the presence of the external lateral force. It can be seen that there is a positive co-relation between $N(J)$ and β with a reasonable r value of 0.69 and p value of 0.027. We also performed the same point-to-point reaching tasks with the *non-dominant* hand for the same subjects. Panel E also shows the co-relation between $N(J)$ and β for the non-dominant hand. In the non-dominant hand, we see positive co-relation between $N(J)$ and β ($r = 0.6$), however the p value of 0.067 indicates no statistical significance between the redundancy and learning rate. This implies that those subjects who use the available redundancy in their dominant hand, learn to adapt to externally applied force faster (see details of the study, statistical analysis and experiments in references [22, 23]). It can also be argued that since the dominant and non-dominant hand are bio-mechanically similar in the context of joint redundancy, the faster learning in the dominant hand is due to active control by the central nervous system.

In section 2 it was shown that for a robotic device with rotary joints, certain directions are "easier" to move than others. In all the point-to-point reaching experiments with the subjects, it was observed that the errors are larger in some directions for a subject – for example, in panel D, it is clear that the errors along 225° clockwise (orange in colour) appear to be larger than along 135° clockwise (green in colour). For a subject, we plot the mean error in the eight directions (shown as circles) and the error bar in each of the 8 directions, and finally fit an ellipse with the mean errors as shown in panel A in figure 8. We can make the following observation:

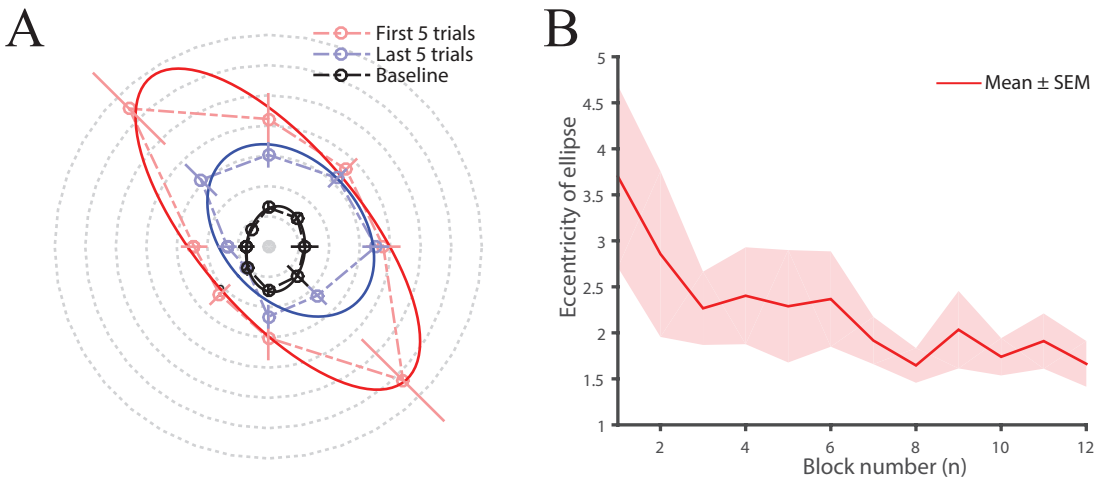

Figure 8: Variation of error along 8 directions for point-to-point reaching task

- The error in the "Baseline" are smaller and the eccentricity of the ellipse is not very large.
- Consistent with panel D in figure 6, the errors are large when the lateral force is applied and as the trials progress, the error decreases – this shows that the subject learns to adapt to the external lateral force.
- Panel B in figure 6 shows the variation of the eccentricity of the ellipse as the trial progresses – the dark solid line is the mean and the shaded region around it shows the standard error mean. It can be clearly seen that the eccentricity of the ellipse decreases as the trials progresses.

It was shown earlier that the increased used of redundancy led to higher learning rate and faster reduction in error. From the above observations one can also argue that the redundancy is used to reduce the increased eccentricity and bring it down to the inherent mechanical anisotropy present in the human arm for point-to-point reaching tasks. Although it is possible to remove anisotropy in mechanical redundant robots, it does not seem to be possible in the redundant human arm. It maybe mentioned that this last result is preliminary and more work needs to be done to arrive at better understanding of the directional nature of learning and use of redundancy in human arm.

4 Conclusion

This work is an attempt to connect redundancy resolution in robotic arms with redundancy resolution in human arm when it is used for point-to-point reaching tasks. In a 30 year old work,

co-authored by Prof. Bernard Roth, it was shown that redundancy can be used to make the end-effector velocity distribution of non-linear serial robot isotropic. From new experimental results obtained in a recent work, it can be argued that the exploitation of redundancy in the human arm results in faster motor learning. Preliminary analysis seem to suggest that the redundancy in the arm is used to make the error in different directions more uniform. More work is required to obtain a better understanding where the redundancy in human arm is processed and how the redundancy in the actuation system, namely muscles, are resolved.

Acknowledgment

The author would like to thank Arkadeep Narayan Chaudhury for help in preparing some of the figures. The experiments with human subjects and the statistical analyses were done by Puneet Singh and are part of his Ph. D. research. The experiments were done at the Centre for Neuro-Science, IISc Bangalore in the laboratory of Aditya Murthy and his help in many aspects of the research is greatly appreciated.

References

[1] Liegeois, A. Automatic supervisory control of the configuration and behavior of multi-body mechanisms. *IEEE Trans. on Systems, Man, and Cybernetics*, **SMC - 7**:868-871, 1977.

[2] Paul R. P. and Stevenson, C. N. Kinematics of robot wrists. *The International Journal of Robotics Research*, **2**(1):31-38, 1983.

[3] Yoshikawa, T. Analysis and control of robotic manipulators with redundancy. In *Robotics Research: The First International Symposium*, Eds. M. Brady and R. Paul, Cambridge, Massachusetts, MIT Press, pp. 735-748, 1984.

[4] Yoshikawa, T. Manipulability and redundancy control of robotic mechanisms. In *Proc. of IEEE Conference on Robotics and Automation*, St. Louis, pp. 1004-1009, 1985.

[5] Rao, C. R. and Mitra, S. K. *Generalized Inverse of Matrices and Its Application.* Wiley, New York, 1977.

[6] Klein, C. A. and Huang, C. H. Review of the pseudo-inverse for the control of kinematically redundant manipulators. *IEEE Trans. on Systems, Man, and Cybernetics*, **SMC-13**(3):245-250, 1983.

[7] Nakamura, Y. *Advanced Robotics: Redundancy and Resolution*, Addison-Wesley, 1991.

[8] Wolf, A., Brown, H. B., Casciola, R., Costa, M., Schwerin, M., Shamas, E. and Choset, H. A mobile hyper-redundant mechanism for search and rescue tasks. In *Proc. of IEEE/RSJ Int. Conference on Intelligent Robots and Systems*, Las Vegas, pp. 2889- 2895, 2003.

[9] Gravagne, I. A. and Walker, I. D. On kinematics of remotely-actuated continuum robots. In *Proc. of IEEE Conference on Robotics and Automation*, San Francisco, pp. 2544-2550, 2000.

[10] Branden, C. and Tooze, J. *Introduction to Protein Structure*, Garland Publishing, New York, 1999.

[11] Chirikjian, G. S. and Burdick, J. W. A modal approach to hyper-redundant manipulator kinematics. *IEEE Trans. on Robotics and Automation*, **10**(3):343-354, 1994.

[12] Zanganeh, K. E. and Angeles, J. The inverse kinematics of hyper-redundant manipulators using splines. *Proc. of IEEE Conference on Robotics and Automation*, Vol. 3, pp. 2797-2802, 1995.

[13] Reznik, D. and Lumelsky, V. Sensor based motion planning in three dimensions for a highly redundant snake robot. *Advanced Robotics*, **9**(3):255-280, 1995.

[14] Sreenivasan, S., Goel, P. and Ghosal, A. A real-time algorithm for simulation of flexible objects and hyper-redundant manipulators. *Mechanism and Machine Theory*, **45**:454-466, 2010.

[15] Ravi, V. C., Rakshit, S. and Ghosal, A. Redundancy resolution using tractrix: Simulations and experiments. *Trans. ASME, Journal of Mechanisms and Robotics*, **2**:031013-1, 2010.

[16] Menon, M. S., Ananthasuresh, G. K. and Ghosal, A. Natural motion of one-dimensional flexible objects using minimization approaches. *Mechanism and Machine Theory*, **67**: 64-76, 2013.

[17] Menon, M. S., Gurumoorthy, B. and Ghosal, A. Efficient simulation and rendering of realistic motion of one-dimensional flexible objects. *CAD Computer Aided Design*, **75-76**:13-26, 2016.

[18] Menon, S. M., Ravi, V. C. and Ghosal, A. Trajectory planning and obstacle avoidance for hyper-redundant serial robots. *Trans. ASME, Journal of Mechanisms and Robotics*, **9**: 0445055-7, 2017.

[19] Ghosal, A. and Roth, B. Instantaneous properties of multi-degrees-of-freedom motions – Point trajectories *Trans. ASME, Journal of Mechanisms, Transmission and Automation in Design*, **19**(1): 107-115, 1987.

[20] Ghosal, A. and Roth, B. A new approach for kinematic resolution of redundancy. *The International Journal of Robotics Research*, **7**(2): 22-35, 1988.

[21] Salisbury, K. *Kinematics and Force Analysis of Articulated Hands.* Ph. D. Thesis, Stanford University, 1982.

[22] Singh, P., Jana, S., Ghosal, A and Murthy, A. Exploration of joint redundancy but not task space variability facilitates supervised motor learning. *Proceedings of the National Academy of Sciences of USA*, **113**(50): 14414-14419, 2016.

[23] Singh, P. *The Role of Basal Ganglia and Redundancy in Supervised Motor Learning.* Ph. D. Thesis, Indian Institute of Science, 2017.

[24] Polhemus LIBERTY, Cochester, Vermont, USA.